The role of stacking faults and twin boundaries in grain refinement of a Cu–Zn alloy processed by high-pressure torsion

Y.B. Wang[a], X.Z. Liao[a,*], Y.H. Zhao[b], E.J. Lavernia[b], S.P. Ringer[c], Z. Horita[d], T.G. Langdon[e,f], Y.T. Zhu[g]

[a] School of Aerospace, Mechanical and Mechatronic Engineering, The University of Sydney, Sydney, NSW 2006, Australia
[b] Department of Chemical Engineering & Materials Science, University of California, Davis, CA 95616, USA
[c] Australian Centre for Microscopy & Microanalysis, The University of Sydney, Sydney, NSW 2006, Australia
[d] Department of Materials Science and Engineering, Faculty of Engineering, Kyushu University, Fukuoka 819-0395, Japan
[e] Departments of Aerospace & Mechanical Engineering and Materials Science, University of Southern California, Los Angeles, CA 90089-1453, USA
[f] Materials Research Group, School of Engineering Sciences, University of Southampton, Southampton SO17 1BJ, UK
[g] Department of Materials Science and Engineering, North Carolina State University, Raleigh, NC 27695, USA

ARTICLE INFO

ABSTRACT

A recent model developed to predict the smallest grain sizes obtainable by severe plastic deformation has worked well for materials with medium to high stacking fault energies (SFEs) but not for those with low SFEs. To probe this issue, experiments were conducted using a Cu–30 wt.% Zn alloy with a very low SFE of 7 mJ/m^2 as the model material. High-pressure torsion was used as the grain refinement technique. The results indicate that stacking faults and twin boundaries play a key role in the grain refinement process such that the smallest achievable grain size is determined by the highest stacking fault and twin density that the system is able to produce. An amorphization of grain boundaries was also observed in the final structure. These observations are very different from those reported for materials having medium to high SFEs and they confirm the operation of a different grain refinement mechanism.

© 2010 Elsevier B.V. All rights reserved.

1. Introduction

Bulk ultrafine-grained (UFG, <1 μm) and nanocrystalline (nc, <100 nm) materials have attracted considerable attention in the past decade because of the potential for achieving unusual mechanical properties including exceptionally high strength without a significant reduction in ductility [1,2] and excellent superplasticity [3]. Recently, severe plastic deformation (SPD) has become one of the most prominent techniques for producing bulk UFG and nc materials because it gives clean and fully dense materials [4]. Several different SPD techniques have been developed including surface mechanical attrition treatment (SMAT) [5], repetitive corrugation and straightening [6], equal channel angular pressing (ECAP) [7] and high-pressure torsion (HPT) [8].

There is always a minimum grain size produced by an SPD process for any specific material. Recently, Mohamed [9] developed a comprehensive model to predict the minimum grain size produced by ball milling. This model is based on a balance between the dislocation generation introduced by ball milling and the dislocation annihilation/recombination produced by thermal processes. Several intrinsic material properties, including the stacking fault energy (SFE), hardness, melting temperature, self-diffusion activation energy and shear modulus, are incorporated into the model. The model can be reformulated in a short form as $d_{min}/b = A(\gamma/Gb)^{0.5}$ [9,10], where d_{min} is the minimum grain size, b is the magnitude of the Burgers vector, A is a constant related to the hardness, melting temperature and self-diffusion activity energy, γ is the SFE and G is the shear modulus. This model has been successful in predicting the minimum grain sizes of materials with medium to high SFEs such as Al, Ni, and Ir but it predicts a significantly larger grain size than produced in ball-milled Ag where the SFE is very low. This discrepancy has been attributed to the decrease in the spacing between two partial dislocations in Ag induced by the severe plastic deformation during ball milling [9]. Some other investigations also documented much smaller grain sizes in alloys with low SFEs processed by various SPD techniques. For example, an average grain size of ~10 nm was reported in a Cu–30 wt.% Zn alloy with a very low SFE of 7 mJ/m^2 processed by HPT [10–12] and this is much smaller than the grain size predicted by the model although a reasonable fit is possible if the exponent of the SFE is increased from 0.5 to 1.37 [10]. Much smaller average grain sizes were reported also in Cu–Al alloys processed by ECAP [13] where

* Corresponding author. Tel.: +61 2 9351 2348; fax: +61 2 9351 7060.
E-mail address: xiaozhou.liao@sydney.edu.au (X.Z. Liao).

these alloys have low SFEs [14]. Since ball-milling is generally considered more effective for grain refinement than ECAP, the results suggest a different grain refinement mechanism may operate in materials having very low SFE.

For materials with medium to high SFEs, dislocation activities play a major role in deformation and grain refinement at low strain rates and at ambient temperature as in the cold rolling of aluminum [15] and the ECAP of copper [16]. During these deformation processes, dislocations propagate, interact, tangle with each other and rearrange spatially to form various sub-structures such as cells and cell blocks [15,17,18]. With increasing strain, the misorientations between neighboring cells and cell blocks increase and the average size of the cell blocks becomes smaller owing to further division. Eventually, the cell-block boundaries become high-angle (>15°) grain boundaries and smaller grains form within the initial coarse grains [19].

For materials with low SFEs, it is expected that deformation twinning will play a significant role in plastic deformation and grain refinement. For example, increasing the Al content in Cu–Al alloys, which simultaneously reduces the SFE, gradually transforms the ECAP-induced grain refinement mechanism from dislocation subdivision to twin fragmentation [13]. A further reduction in the grain size to the nanometer regime also promotes deformation twinning. Thus, a very high density of deformation twins was present in nanocrystalline Cu deformed under a very low strain rate at room temperature whereas no twin were visible in UFG Cu deformed under the same condition [20]. It has been shown that these twins in nc Cu were formed via partial dislocation emission from the grain boundaries [21–24].

Because both a low SFE and an nc structure promote deformation twinning, it is reasonable to anticipate that the combination of low SFE and an nc grain size will give a very high density of deformation twins. However, experimental results for HPT Cu–Zn alloys suggested otherwise. While the reported experimental results showed a significant effect of SFE on the final grain size achievable by HPT, such that a reduction in the SFE reduced the final HPT grain size to a value significantly smaller than predicted by the theoretical model, the density of deformation twins in the HPT alloys with nc grains was very low [10,12].

These results raise some important questions. Specifically, it is necessary to determine (i) why a lowering of the SFE reduces the final HPT grain size, (ii) why the final grain size in materials with low SFEs is significantly smaller than the theoretical prediction and (iii) why the measured density of deformation twins is very low in the final nc structure. It is important to note also that amorphous grain boundaries were readily observed in HPT nc Cu–Zn alloys [10–12] but the formation mechanism for these amorphous boundaries is not understood. Furthermore, amorphous structures usually form in complex multi-element systems and not in simple alloys such as the Cu–Zn system. These important questions require a comprehensive evaluation of the process of SPD-induced grain refinement of materials having low SFEs.

In the present study, a systematic transmission electron microscopy (TEM) investigation was conducted on a Cu–30 wt.% Zn alloy subjected to 5 revolutions by HPT at room temperature under a low strain rate. Because the value of the shear strain is linearly proportional to the radius r in the HPT disk [25], it was possible to observe different deformation stages from UFG to nc grain sizes by selecting different positions on the 5 revolution disk. In this way it was feasible to evaluate the microstructural evolution processes induced by HPT using a single disk.

2. Experimental procedure

A commercial Cu–30 wt.% Zn rod with a diameter of 10 mm was used in this investigation. A disk with a thickness of 1.2 mm was

cut from the rod. The disk was ground on both sides using abrasive papers until its thickness reached ~0.80 mm. The disk was then placed between a stationary upper anvil and a rotational lower anvil and processed using an HPT facility [26] at room temperature for 5 rotations at a speed of 1 rotation/min under an imposed pressure of 5.0 GPa. Thus, the HPT disk was subjected concurrently to a high pressure and torsional straining. Since the processing operation was conducted under quasi-constrained conditions [8], the thickness of the disk was reduced during processing to ~0.78 mm.

After HPT processing, 5 samples were prepared for evaluation by transmission electron microscopy (TEM) by cutting from the center to the edge of the HPT disk along a radial direction. Specifically, a strip with a width of ~3 mm was cut across the diameter of the disk and this strip was then further cut into small rectangular pieces, each ~1 mm in width, with the first cut positioned on the center of the disk and the remaining four pieces located at increasing distances from the center to the edge. These samples were thinned to a thickness of ~30 μm by mechanically grinding from both sides using abrasive papers (800–2000 grade). Further thinning was performed with a Gatan dimple grinder followed by ion-beam thinning using a Fischione 3000 system with an Ar+ accelerating voltage of 4 kV. Liquid nitrogen was used to prevent any heating of the TEM specimens during the ion-beam thinning process.

All TEM observations were made in the plane of the disk and the microstructural evolution was conducted using a JEM-3000F microscope operating at a voltage of 300 kV. Bright-field diffraction contrast, high-resolution phase contrast imaging and selected area electron diffraction (SAED) techniques were applied in the experiments. High-resolution imaging was performed by tilting samples to a ⟨1 1 0⟩ zone axis. Some high-resolution images were processed using Fourier and inverse-Fourier transformation to improve their image quality for easy analysis. The dislocations in experimental high-resolution TEM images and their corresponding Fourier-filtered TEM images were identified by determining the ends of the half atomic planes along {1 1 1} planes. To prevent any potential artifact introduced by image processing, defects identified in Fourier-filtered images were double-checked with their original experimental images. Grain sizes were determined directly from the TEM images by measuring the widths of individual grains along linear traverses. The average grain sizes were estimated at each deformation stage by counting at least two hundred randomly selected grains.

3. Results

3.1. Presence of three distinct microstructures

Fig. 1a, c, and e shows typical TEM bright-field images taken from the central area, half-way to the edge and at the edge of the HPT disk, respectively. These images represent three typical stages in the microstructural evolution and henceforth they are designated deformation stages I, II and III, respectively. The corresponding SAED patterns are posted at the upper right corner of each image. Fig. 1b, d, and f shows the grain size distribution histograms for these three stages. In stage I in Fig. 1a the microstructure is characterized by equiaxed ultrafine grains although twins are visible occasionally in some small grains as also reported in earlier observations [10–12]. The SAED pattern in Fig. 1a was obtained from many ultrafine grains by using a large selected area aperture, which selects an area with a diameter of 1.25 μm, and it suggests a random distribution of grain orientations. The grain sizes in stage I spread from ~40 to 400 nm as shown in Fig. 1b with an average grain size of ~190 nm.

In stage II in Fig. 1c the microstructure is dominated by the formation of an elongated plate-like structure having aspect ratios
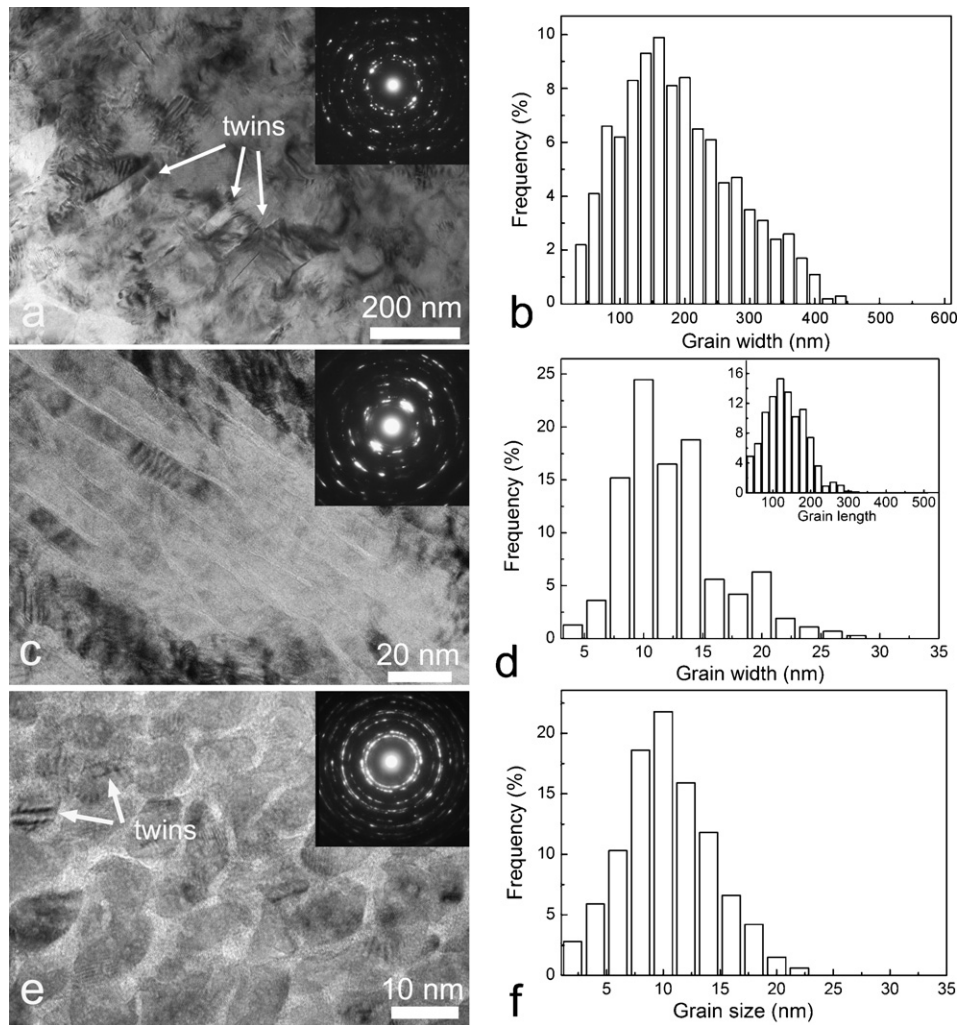
Fig. 1. Typical TEM images (a, c and e) and grain size distributions (b, d and f) of three distinct microstructures at different stages of HPT processing. Insets in the TEM images are their corresponding SAED patterns. Twins visible in (a) and (e) are indicated.

of length to width of up to ~20. The corresponding SAED pattern, which was obtained from a group of plates with parallel boundaries, suggests a group of {1 1 1} planes of the elongated grains lie approximately parallel to each other with some misorientation. The length and the width distributions of the elongated plate-like grains are shown in the histograms in Fig. 1d. These measurements reveal a narrow width distribution of ~5–30 nm with an average width of ~13 nm and a larger length distribution of ~40–300 nm with an average length of ~130 nm. The length distribution is therefore similar to the grain size distribution in stage I although there was only a small number of elongated grains with lengths longer than ~200 nm.

In stage III in Fig. 1e nanocrystalline grains with an equiaxed morphology and amorphous grain boundaries co-exist. The grain sizes in this condition range from ~2 to 22 nm in Fig. 1f with an average size of ~10 nm where this is comparable to the widths of the grains in stage II. The SAED pattern in Fig. 1e shows continuous rings thereby indicating the random orientations of the grains in stage III. Twins were seen only occasionally in stage III as indicated in two grains in Fig. 1e.

3.2. Microstructural evolution from stage I to stage II

Fig. 2 shows microstructures between stages I and II. A high density of parallel lines with line intervals of ~5–20 nm were visible in

some equiaxed grains and high-resolution TEM images confirmed these parallel lines are stacking faults or very narrow nanotwins. An example of a high density of stacking faults is shown in Fig. 2a. Fig. 2b shows a magnified image of part of Fig. 2a (indicated using a white rectangle) and a high-resolution TEM image of a stacking fault in the inset at the upper right corner of the figure. While there are a few stacking faults passing through the whole grain, most of these stacking faults have one end pinned at the grain boundary and the other end stops in the grain interior, as indicated by white arrowheads in Fig. 2b. In some occasional cases, stacking faults are also seen with their two ends located within a grain and one example is marked with a black arrowhead in Fig. 2b. These observed stacking fault morphologies suggest that most of the stacking faults were formed through partial dislocation emission from grain boundaries while a few may have formed through a perfect dislocation disassociation into two partial dislocations. Fig. 2c shows an example of nanotwins in a grain where the twin relationship is confirmed by the SAED pattern in Fig. 2c. While many twins pass through the whole grain with grain sizes larger than ~200 nm, there are two twins having one end located at the grain boundary (GB) and the other end terminated within the grain as indicated by white arrowheads in Fig. 2c. Fig. 2d further magnifies the area indicated by a white rectangle in Fig. 2c and shows two twins, denoted by white arrowheads, terminating within the grain.
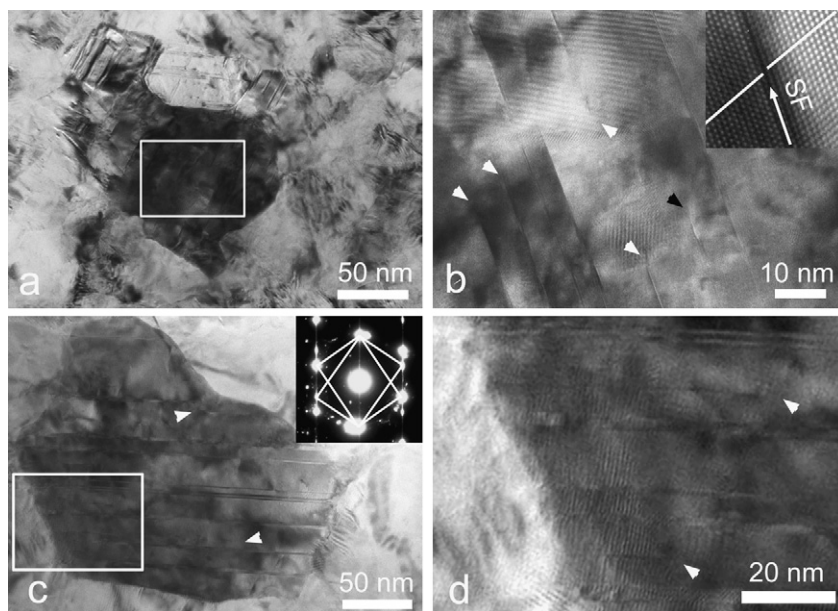
Fig. 2. (a) A typical TEM image of a grain with a high density of stacking faults, (b) a high resolution TEM image of part of (a), (c) a grain with a high density of nanotwins and its corresponding ⟨1 1 0⟩ SAED pattern showing the twin relationship and (d) an enlarged image of the area marked with a rectangle in (c). White arrowheads mark the places where stacking faults and twins terminate in grains. A black arrowhead indicates a stacking fault with the two ends terminating within a grain.

The morphologies of twins and stacking faults shown in Fig. 2 suggest that the twins and most stacking faults originate through partial dislocation emission from the GBs [27]. It has been proposed that partials can multiply at the boundaries of nano-grains via a cross-slip mechanism to produce the deformation twins [28]. While stacking faults may form occasionally via the dissociation of perfect dislocations, this mechanism does not apply to the formation of the twins observed in this investigation because the possibility for accidental overlapping of dissociated partial dislocations on neighboring {1 1 1} planes is very low [29].

Fig. 3a was also taken between stages I and II and it shows two grains labeled "A" and "B" with grain sizes of ∼200 nm and having fine lamellar structures with different lamella thicknesses within the grains. The inset ⟨0 1 1⟩ SAED pattern taken from grain B presents two ⟨0 1 1⟩ reciprocal lattices forming a twin relationship, thereby showing the lamellae are nano-deformation twins. Careful examination of a large number of grains at this deformation stage by tilting the grains to a ⟨0 1 1⟩ orientation suggested that nanotwins and/or stacking faults were present in most of the grains and only a small fraction of the grains were free of twins and stacking faults. Compared with the structure in stage I shown in Fig. 1a, in which stacking faults and twins are only seen occasionally, much higher densities of stacking faults and twins were visible in this transition stage. Similar to the situation in Fig. 2, many stacking faults and twins were also visible originating from GBs and terminating within the grains. The thicknesses of the twin lamellae in Fig. 3 are ∼10–20 nm. With the increase in shear strain at this greater distance from the center of the disk, the twin density further increases and this reduces the thicknesses of the twin lamellae to ∼10 nm. At the same time, twin boundaries (TBs) start to curve and this gives deviations from the strict crystallographic twin relationship and forms incoherent TBs. The curved TBs are made visible in Fig. 3b, which is a magnified image of part of grain B in Fig. 3a, by drawing two straight lines parallel to the left end and right end of the same TB, respectively. Thus, the two straight lines are non-parallel and the curved TB leads to a deviation from the strict crystallographic twin relationship between the twins and the matrix. This is also verified by the SAED pattern inserted in Fig. 3a in which the diffraction spots become elongated arcs with a spreading angle of up to 7°. In addition, super-thin secondary twins and stacking

faults also start to form within some incoherent twin lamellae at this stage along another {1 1 1} group, as indicated by the white arrowheads in Fig. 3b. This is an important step towards the formation of equiaxed grains in the later stages of deformation which is discussed later.

The accumulation of dislocations at the TBs is responsible for the TB curvature. It has been reported that TBs are effective barriers for dislocation motion [30] and this was confirmed in the present sample. Fig. 4 shows a high-resolution TEM image of a curved TB with a very high density of dislocations accumulated at the boundary. The dislocations marked with white "T" traveled along the {1 1 1} planes that intersect with the TB and stopped in front of the TB. The dislocations marked with black "T" traveled along the {1 1 1} planes that were originally parallel to the TB. However, these dislocations were not blocked by the TB but, because of the dislocation tangling effect, their motion was also stopped in this area of high dislocation density. With the accumulation of the dislocations at the TB, the {1 1 1} planes at the two sides of the TB are no longer parallel to each other but they have a deviation angle of about 8°. This 8° deviation is indicated in Fig. 4 by drawing two white lines parallel to the (1 1 1) of the twin (marked as $(1\,1\,1)_T$) and the matrix (marked as $(1\,1\,1)_M$) and then measuring the angle between these lines. The main contribution to this deviation comes from the white dislocations, which is confirmed by the calculation $\theta = b/D = 7°$, where θ is the deviation angle, b is the length of the Burgers vector of the white dislocations and D is the average spacing between neighboring white dislocations.

It should be noted that, while the white dislocations in Fig. 4 are geometrically necessary dislocations that accommodate the geometrical deviation from the coherent twin relationship, some black dislocations with opposite Burgers vectors do not contribute to the crystallographic misorientation because their strain fields cancel each other. The presence of these non-geometrically necessary dislocations at the GBs makes the boundaries non-equilibrium in character, as has been widely reported for microstructures produced by SPD [31–34].

In addition to deviating from the crystallographic twin relationship, bent incoherent TBs also act as sources of emitting dislocations. A recent *in situ* tensile TEM investigation of Cu with growth twins revealed that TBs serve not only as strong barriers
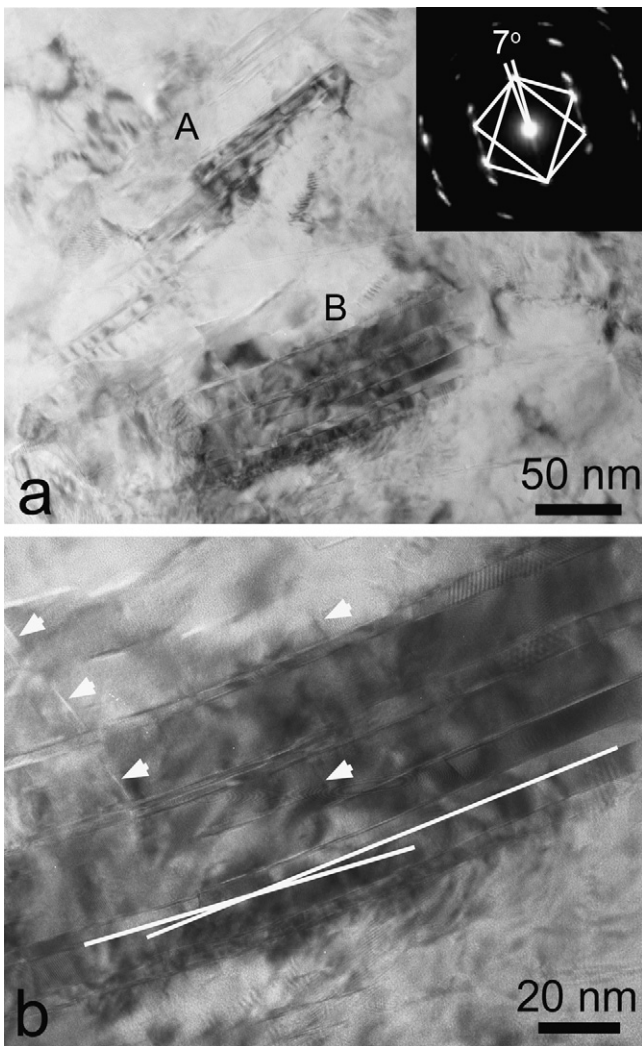
Fig. 3. (a) Twin bundles marked by letters A and B, respectively. Inset in (a) is an SAED pattern taken from area B showing a 7° deviation from the strict twin relationship; (b) an enlarged image of the twin bundle B. Two straight lines, which are parallel to the left and right ends of one TB, respectively, were drawn to indicate the curvature of the TBs. Secondary twins are indicated using white arrowheads.
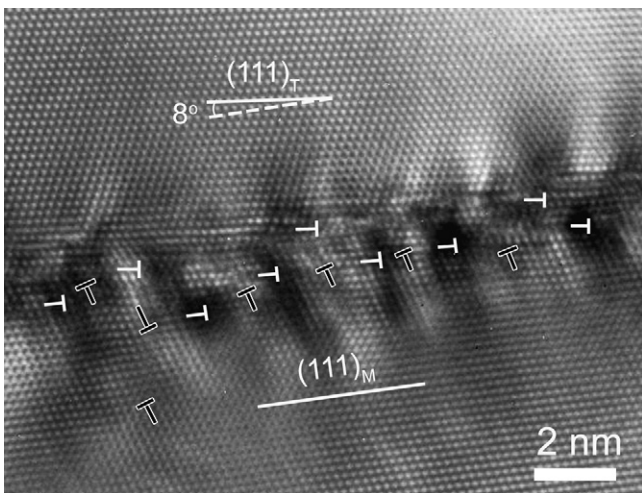

Fig. 4. A high resolution TEM image of a bent TB showing a high density of dislocations, which are indicated using white and black "T", accumulated at the TB. Two white solid lines were drawn parallel to {1 1 1} at each side of the TB, respectively, and one dash white line was also drawn parallel to $(1 1 1)_M$ to indicate the misorientation between the {1 1 1} planes across the TB.
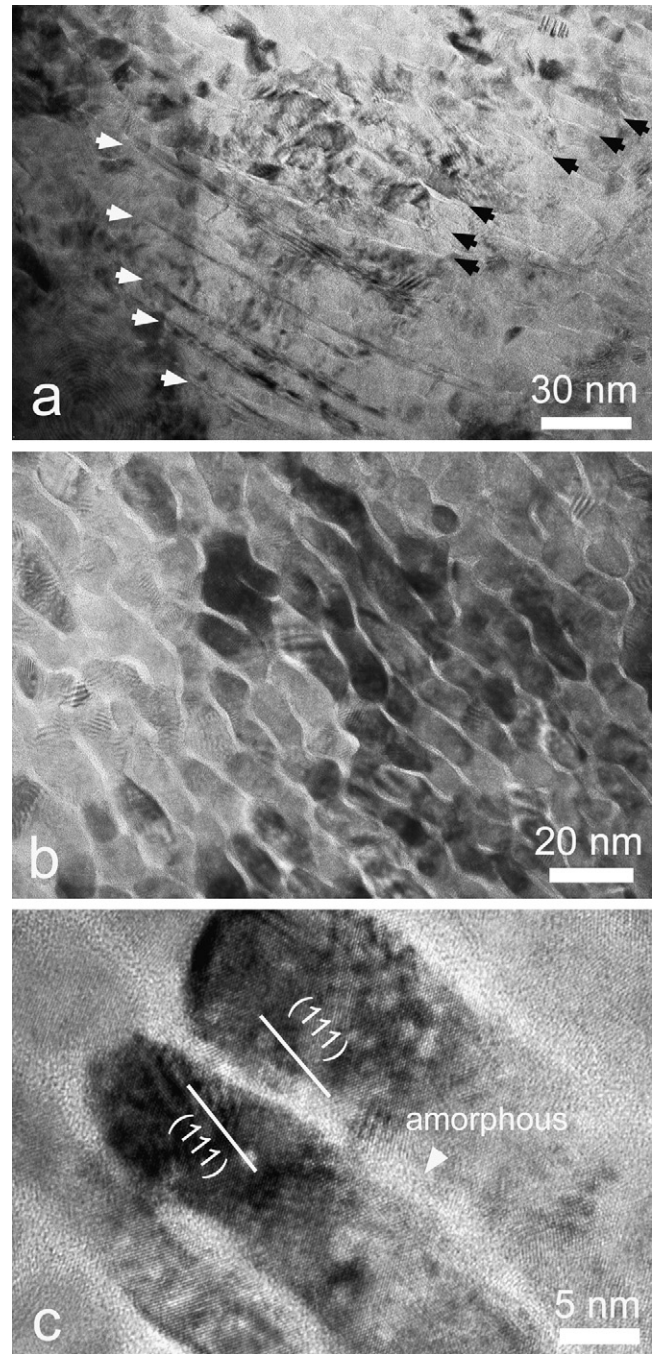

Fig. 5. (a) A TEM image with bent twin lamellae marked by white arrowheads in the lower left of the image and the boundaries of elongated grains marked by black arrowheads at the upper right, (b) a magnified image of the elongated grains with GBs of an amorphous structure; (c) a high-resolution image of two elongated grains. Two white lines are drawn to indicate the {1 1 1} planes in the grains.

to dislocation movement but also as dislocation emission sources [35]. These dislocations emitted from bent TBs will dissociate into two Shockley partial dislocations connected by a stacking fault [36] and, as a result, the TBs and stacking faults will divide the larger grains into smaller rhombic domains which act as precursors for additional grain refinement. This is discussed further in Section 4.

The accumulation of a high density of dislocations not only transforms originally coherent twin boundaries into incoherent high-angle GBs but also leads to an amorphization at the GBs in the transition from stage I to stage II. An example of GB amorphization is shown in Fig. 5. Twins with bent TBs, as marked with white
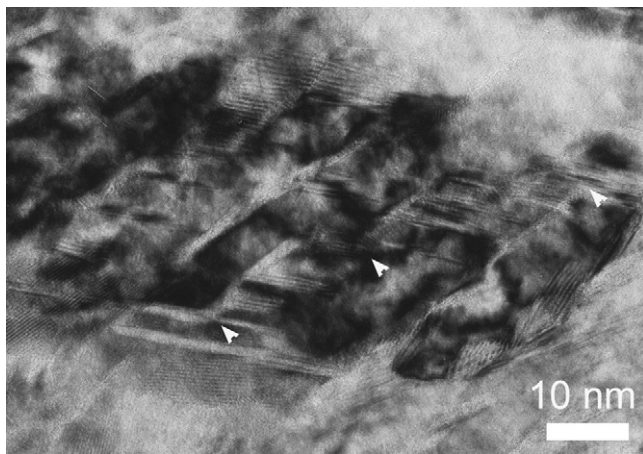
Fig. 6. A TEM image showing seconding twins intersecting elongated grains; white arrowheads mark the places where secondary twins traverse the previous elongated twins.

Fig. 7. Schematic illustration of the grain refinement mechanism for the Cu–30 wt.% Zn alloy processed by HPT.

arrowheads, are visible at the lower left in Fig. 5a. At the upper right of Fig. 5a, boundaries marked by black arrowheads, which are approximately parallel to the TBs at the lower left of the figure, are broadened and appear with bright contrast. A magnified image of this type of boundary is shown in Fig. 5b indicating that the boundaries have an amorphous structure. Furthermore, the amorphous structure is seen more clearly from a high-resolution TEM image of the area shown in Fig. 5c between two elongated grains. A (1 1 1) plane is marked with a white line in each of the two grains, revealing a slight misorientation (about 5°) between the two marked (1 1 1) planes. This implies that the amorphization is probably related to stacking faults or twins.

3.3. Microstructural evolution from stage II to stage III

Fig. 3b showed some evidence for the formation of secondary stacking faults and ultra-thin twins at the transition stage from stage I to stage II. With increasing shear strain, as at the transition from stage II to stage III, these secondary stacking faults and thin twins became thickened as shown in Fig. 6. It should be noted that some of these "secondary" twins traverse "primary" elongated twins (marked with white arrowheads) that block the "primary" TBs, thereby indicating that these "secondary" twins were formed simultaneously with the "primary" twins. The secondary stacking faults and twins divide the previously elongated grains into many equiaxed parts and this transforms the elongated structure into an equiaxed nanocrystalline structure. Following the evolution track of the primary TBs, secondary TBs also evolved into high-angle GBs with the amorphous structure located at the boundaries as is evident in Fig. 1e.

4. Discussion

Based on the three distinct microstructures, designated stages I, II and III, and the intermediate transitional structures observed between the center and the edge of the HPT disk, it is now feasible to propose a mechanism for grain refinement in materials processed by HPT and having very low SFEs. This mechanism is illustrated schematically in Fig. 7 and described in detail in the following section.

4.1. Grain subdivision and refinement via TBs and stacking faults

Recent reports have shown that the SFE has a significant effect on the final grain sizes achieved in materials processed by HPT
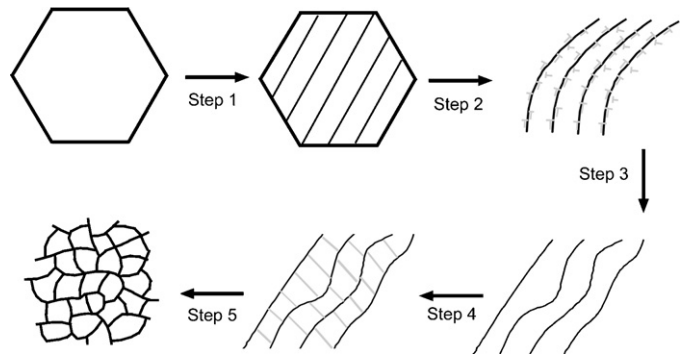
[10–13,27,37–39]. Decreasing the SFE by alloying reduces the final grain size that may be attained when using identical HPT processing conditions. For example, under the same processing conditions, pure Cu, Cu–10 wt.% Zn, and Cu–30 wt.% Zn have average measured grain sizes of ~75, ~50 and ~10 nm, respectively [10,12]. Nevertheless, the precise effect of the SFE on grain refinement is not yet understood. The present experiments show that equiaxed UFG crystals become divided into twin lamellae with average thicknesses of ~13 nm through partial dislocation emissions from GBs (step 1 in Fig. 7). Because of the low SFE of the Cu–30 wt.% Zn alloy, these partial dislocation emissions occur readily in UFG crystals during SPD [27] and the density of the deformation twins increases with increasing strain until, in the present alloy, the average twin lamella thickness reaches ~13 nm. In practice, it is recognized that the minimum twin lamella thickness will be a function of the SFE because a decrease in the SFE increases the twin density and thereby reduces the average twin lamella thickness.

The increase in shear strain, which is manifest across the HPT disk from the center to the edge, is associated with an increase in the density of stacking faults and twins and also with an increase in the dislocation density. Some of these dislocations pile up at TBs because TBs are strong obstacles for dislocation slip [30,35]. This dislocation accumulation at the TBs serves to bend the original atomically-flat coherent TBs (step 2 in Fig. 7) and transform the TBs into incoherent TBs. Further straining transforms the incoherent TBs into high-angle GBs (step 3 in Fig. 7).

Earlier *in situ* TEM observations [35] showed that the interaction between TBs and dislocations not only transforms the TBs into high-angle GBs but also generates new dislocation sources at the GBs. As a result, partial dislocations are emitted from the new GBs with further deformation and secondary deformation twins are formed such that the intersection between these twins and the new GBs produce rhombic domains (step 4 in Fig. 7). It is important to emphasize that the TBs/GBs intersection is a crucial development for the occurrence of grain subdivision in the Cu–30 wt.% Zn alloy. Apparently, these TBs/GBs intersections subdivide the original grains efficiently and lead to the formation of the new refined microstructure. Further deformation transforms the secondary TBs into incoherent high-angle GBs as noted earlier for the primary TBs. In this grain size range, grain rotation probably plays a significant role in plastic deformation [40,41] thereby producing a final nc structure having a random grain orientation (step 5 in Fig. 7).

It is reasonable to anticipate that the preceding grain refinement mechanism, as delineated in Fig. 7, will be common for all FCC materials having low SFEs. The mechanism is similar to the grain refinement mechanism of FCC metals and alloys processed under extreme conditions of very high strain rates and/or very low

temperatures because both high strain rates and low temperatures also promote extensive deformation twinning [42]. Typical examples of this effect include Cu and stainless steel processed by SMAT [43–46] and dynamic plastic deformation [47].

The model of Mohamed [9] for the minimum grain size, d_{min}, achieved in ball milling is based on a balance between the rate of hardening and the rate of recovery [48]. Specifically, the model assumes that grain refinement involves three stages [49]: (1) a localization of the high dislocation density in shear bands, (2) the formation of cells and subgrains through dislocation interactions, and (3) the transformation of subgrain boundaries into high-angle grain boundaries through dislocation accumulations at the boundaries. In practice, these three stages have been widely documented in FCC materials having medium to high SFEs [15,19,50]. Although HPT and ball milling are two different straining processes that differ in strain rate and force parameters, the Mohamed model [9] was originally applied to ball milled materials and is relevant to HPT since the principles used in the model also apply to the HPT process. However, it is apparent from the present investigation that the grain refinement process in materials with low SFEs, as with the Cu−30 wt.% Zn alloy, is different from the three stages assumed in the conventional model. This difference provides an immediate explanation for the observation that experimental data from materials with medium to high SFEs fit very well with the model whereas significant deviations are observed in materials with low SFEs.

4.2. Local amorphization at TBs and their neighboring areas

The grain boundaries of the nc grains are of an amorphous structure, as is evident in Fig. 1e. Figs. 4 and 5c show dislocation accumulation at a TB and amorphization of TBs, respectively, suggesting a possible link between dislocation accumulation at TBs and the formation of the amorphous structure. Indeed, detailed experimental observations show that the amorphous structure always nucleated at TBs and high densities of dislocations frequently accompany the embryos of the amorphous structure, as shown in Fig. 8a in which the TBs are indicated and dislocations are marked with black "T". The areas with white contrast in Fig. 8a are of an amorphous structure with high densities of dislocations. Although the amorphous structure nucleated from TBs, the structure grew not only along the TBs but also extended into the interior of grains to form curved amorphous GBs. An example is shown in the area marked with a white rectangle in Fig. 8a and a magnified Fourier-filtered image of this area is shown in Fig. 8b. A very high density of dislocations also exists in the area of the curved amorphous GB where the dislocations are indicated by "T" symbols. It is expected that the dislocation accumulation originated from the TBs. However, because dislocations distribute in a complex way in 3-dimensional space, the dislocation accumulation and tangling can easily extend to other areas neighboring the TBs leading to the spatial distribution of dislocations shown in Fig. 8b. A previous investigation on a deformed TiNi alloy also shows that an amorphous phase nucleated at TBs because of the accumulation of a high density of dislocations at TBs [51].

Local amorphization induced by dislocation accumulation was also reported in NiTi alloys [52–55], a CuZrTi alloy [56] and an Al alloy [57] processed by severe plastic deformation. Dislocation accumulation introduces significant elastic strain which has been theoretically proven to play a critical role in the nucleation of an amorphous structure at dislocation cores [58]. The formation of the amorphous structure effectively releases the high elastic strain in an area with a high density of dislocations and thereby reduces the energy of the system. Molecular dynamics simulations [59,60] demonstrated that crystalline defects contribute directly to atomic position disorder and lattice strain, leading to a softening of the elastic modulus and a final collapse of the crystallinity. It should be
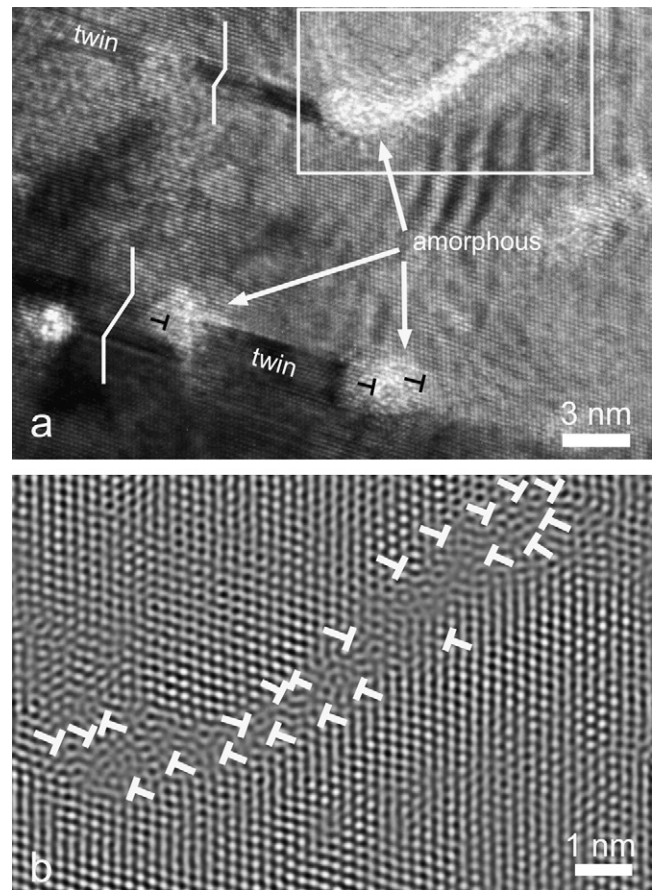

Fig. 8. (a) A TEM image showing nano-twin lamellae and the nucleation and growth of the amorphous structure at TBs where zigzag white lines mark the {1 1 1} planes that form the twin relationship; (b) an enlarged Fourier-filtered image of the area marked with a white rectangle in (a) showing a high density of dislocations at the amorphous area. Dislocations are marked with black and white "T".

noted that amorphization only occurs locally because the distribution of dislocations is highly localized.

5. Summary

The evolution process of the microstructure of a Cu−30 wt.% Zn alloy with a low SFE processed by HPT was investigated using TEM. The reason for a significant deviation between the theoretical prediction and experimental data for the HPT-induced minimum grain size was analyzed. The following conclusions were reached:

1. Deformation twins and stacking faults play a key role in HPT-induced grain refinement. The finest grain size is determined by the highest stacking fault/twin density that the system is able to produce.
2. Equiaxed ultrafine grains with grain sizes of hundreds of nanometers were refined through the formation of a high density of stacking faults and twins, giving elongated grains with high aspect ratios of length to width.
3. With the accumulation of a high density of dislocations at stacking faults and twin boundaries, the original atomically-flat coherent stacking faults and twin boundaries evolved into curved incoherent high angle grain boundaries from which secondary stacking faults and twins were emitted.
4. The emission of secondary stacking faults and twins further refined the grains and transformed the elongated grains into equiaxed grains having a grain size of ∼10 nm.

5. The density of deformation twins is very low in the final nc structure because most TBs have transformed to conventional high-angle GBs.
6. The significant deviation between the theoretical prediction and experimental data on the HPT-induced minimum grain size arises from a discrepancy between the grain refinement mechanism assumed in the theory and the refinement mechanism operating in the Cu–30 wt.% Zn alloy.
7. An amorphous structure was formed at the nanocrystalline grain boundaries through an accumulation of dislocations at twin boundaries which subsequently transformed these boundaries into incoherent grain boundaries.

Acknowledgements

References

[1] R.Z. Valiev, I.V. Alexandrov, Y.T. Zhu, T.C. Lowe, J. Mater. Res. 17 (2002) 5.
[2] K.M. Youssef, R.O. Scattergood, K.L. Murty, J.A. Horton, C.C. Koch, Appl. Phys. Lett. 87 (2005) 091904.
[3] Z. Horita, T.G. Langdon, Scripta Mater. 58 (2008) 1029.
[4] R.Z. Valiev, R.K. Islamgaliev, I.V. Alexandrov, Prog. Mater. Sci. 45 (2000) 103.
[5] K. Lu, J. Lu, J. Mater. Sci. Technol. 15 (1999) 193.
[6] J.Y. Huang, Y.T. Zhu, H. Jiang, T.C. Lowe, Acta Mater. 49 (2001) 1497.
[7] R.Z. Valiev, T.G. Langdon, Prog. Mater. Sci. 51 (2006) 881.
[8] A.P. Zhilyaev, T.G. Langdon, Prog. Mater. Sci. 53 (2008) 893.
[9] F.A. Mohamed, Acta Mater. 51 (2003) 4107.
[10] Y.H. Zhao, X.Z. Liao, Y.T. Zhu, Z. Horita, T.G. Langdon, Mater. Sci. Eng. A 410–411 (2005) 188.
[11] Y.H. Zhao, Y.T. Zhu, X.Z. Liao, Z. Horita, T.G. Langdon, Appl. Phys. Lett. 89 (2006) 121906.
[12] L. Balogh, T. Ungár, Y.H. Zhao, Y.T. Zhu, Z. Horita, C. Xu, T.G. Langdon, Acta Mater. 56 (2008) 809.
[13] S. Qu, X.H. An, H.J. Yang, C.X. Huang, G. Yang, Q.S. Zang, Z.G. Wang, S.D. Wu, Z.F. Zhang, Acta Mater. 57 (2009) 1586.
[14] A. Orlová, M. Pahutová, J. Čadek, Philos. Mag. 23 (1971) 303.
[15] Q. Liu, D. Juul Jensen, N. Hansen, Acta Mater. 46 (1998) 5819.
[16] F. Dalla Torre, R. Lapovok, J. Sandlin, P.F. Thomson, C.H.J. Davies, E.V. Pereloma, Acta Mater. 52 (2004) 4819.
[17] Y.B. Wang, X.Z. Liao, Y.T. Zhu, Int. J. Mater. Res. 100 (2009) 1632.
[18] T. Ungár, J. Gubicza, G. Ribárik, A. Borbély, J. Appl. Cryst. 34 (2001) 298.
[19] D.A. Hughes, N. Hansen, Acta Mater. 45 (1997) 3871.
[20] X.Z. Liao, Y.H. Zhao, S.G. Srinivasan, Y.T. Zhu, R.Z. Valiev, D.V. Gunderov, Appl. Phys. Lett. 84 (2004) 592.
[21] V. Yamakov, D. Wolf, S.R. Phillpot, H. Gleiter, Acta Mater. 50 (2002) 5005.
[22] V. Yamakov, D. Wolf, S.R. Phillpot, A. Mukherjee, H. Gleiter, Nature Mater. 1 (2002) 1.
[23] D. Wolf, V. Yamakov, S.R. Phillpot, A. Mukherjee, H. Gleiter, Acta Mater. 53 (2005) 1.
[24] H. Van Swygenhoven, P.M. Derlet, A.G. Frøseth, Nature Mater. 3 (2004) 399.
[25] A.P. Zhilyaev, G.V. Nurislamova, B.K. Kim, M.D. Baró, J.A. Szpunar, T.G. Langdon, Acta Mater. 51 (2003) 753.
[26] G. Sakai, Z. Horita, T.G. Langdon, Mater. Sci. Eng. A 393 (2005) 344.
[27] Z.W. Wang, Y.B. Wang, X.Z. Liao, Y.H. Zhao, E.J. Lavernia, Y.T. Zhu, Z. Horita, T.G. Langdon, Scripta Mater. 60 (2009) 52.
[28] Y.T. Zhu, X.L. Wu, X.Z. Liao, J. Narayan, S.N. Mathaudhu, L.J. Kecskés, Appl. Phys. Lett. 95 (2009) 031909.
[29] X.Z. Liao, F. Zhou, E.J. Lavernia, S.G. Srinivasan, M.I. Baskes, D.W. He, Y.T. Zhu, Appl. Phys. Lett. 83 (2003) 632.
[30] L. Lu, Y.F. Shen, X.H. Chen, L.H. Qian, K. Lu, Science 304 (2004) 422.
[31] A.A. Nazarov, A.E. Romanov, R.Z. Valiev, Acta Metall. Mater. 41 (1993) 1033.
[32] Z. Horita, D.J. Smith, M. Furukawa, M. Nemoto, R.Z. Valiev, T.G. Langdon, J. Mater. Res. 11 (1996) 1880.
[33] K. Oh-ishi, Z. Horita, D.J. Smith, T.G. Langdon, J. Mater. Res. 16 (2001) 583.
[34] X.Z. Liao, Y.H. Zhao, Y.T. Zhu, R.Z. Valiev, D.V. Gunderov, J. Appl. Phys. 96 (2004) 636.
[35] Y.B. Wang, B. Wu, M.L. Sui, Appl. Phys. Lett. 93 (2008) 041906.
[36] Y.B. Wang, M.L. Sui, Appl. Phys. Lett. 94 (2009) 021909.
[37] Y.H. Zhao, X.Z. Liao, T.G. Langdon, Y.T. Zhu, Mater. Sci. Eng. A 474 (2008) 342.
[38] Y.H. Zhao, X.Z. Liao, Z. Horita, T.G. Langdon, Y.T. Zhu, Mater. Sci. Eng. A 493 (2008) 123.
[39] T. Ungár, L. Balogh, Y.T. Zhu, Z. Horita, C. Xu, T.G. Langdon, Mater. Sci. Eng. A 444 (2007) 153.
[40] M. Ke, S.A. Hackney, W.W. Milligan, E.C. Aifantis, Nanostruct. Mater. 5 (1995) 689.
[41] Y.B. Wang, B.Q. Li, S.X. Mao, M.L. Sui, Appl. Phys. Lett. 92 (2008) 011903.
[42] J.W. Christian, S. Mahajan, Prog. Mater. Sci. 39 (1995) 1.
[43] K. Wang, N.R. Tao, G. Liu, J. Lu, K. Lu, Acta Mater. 54 (2006) 5281.
[44] N.R. Tao, H.W. Zhang, J. Lu, K. Lu, Mater. Trans. 44 (2003) 1919.
[45] H.W. Zhang, Z.K. Hei, G. Liu, J. Lu, K. Lu, Acta Mater. 51 (2003) 1871.
[46] N.R. Tao, K. Lu, Scripta Mater. 60 (2009) 1039.
[47] Y.S. Li, N.R. Tao, K. Lu, Acta Mater. 56 (2008) 2429.
[48] J. Eckert, J.C. Holzer, C.E. Krill, W.L. Johnson, J. Mater. Res. 7 (1992) 1751.
[49] H.J. Fecht, Nanostruct. Mater. 6 (1995) 33.
[50] X.Z. Liao, J.Y. Huang, Y.T. Zhu, F. Zhou, E.J. Lavernia, Philos. Mag. 83 (2003) 3065.
[51] E.V. Tatyanin, V.G. Kurdyumov, Phys. Stat. Sol. (a) 121 (1990) 455.
[52] A.V. Sergueeva, C. Song, R.Z. Valiev, A.K. Mukherjee, Mater. Sci. Eng. A 339 (2003) 159.
[53] J.Y. Huang, Y.T. Zhu, X.Z. Liao, R.Z. Valiev, Philos. Mag. Lett. 84 (2004) 183.
[54] M. Peterlechner, T. Waitz, H.P. Karnthaler, Scripta Mater. 60 (2009) 1137.
[55] K. Inaekyan, V. Brailovski, S. Prokoshkin, A. Korotitskiy, A. Glezer, J. Alloys Compd. 473 (2009) 71.
[56] Á. Révész, S. Hóbor, J.L. Lábár, A.P. Zhilyaev, Z. Kovács, J. Appl. Phys. 100 (2006) 103522.
[57] X. Wu, N. Tao, Y. Hong, J. Lu, K. Lu, J. Phys. D: Appl. Phys. 38 (2005) 4140.
[58] I.A. Ovid'ko, A.B. Reizis, J. Phys. D: Appl. Phys. 32 (1999) 2833.
[59] H. Ikeda, Y. Qi, T. Cagin, K. Samwer, W.L. Johnson, W.A. Goddard, Phys. Rev. Lett. 82 (1999) 2900.
[60] M. Li, Phys. Rev. B 62 (2000) 13979.